Deformation in a partially molten mantle: Constraints from plagioclase lherzolites from Lanzo, western Alps

Katherine Higgie, Andrea Tommasi

Deformation in a partially molten mantle: Constraints from plagioclase lherzolites from Lanzo, western Alps

Katherine Higgie, Andréa Tommasi *

Geosciences Montpellier, CNRS & Université de Montpellier 2, F-34095 Montpellier cedex 5, France

We studied the deformation in a partially molten mantle through detailed petrostructural analysis of plagioclase lherzolites from the northwestern part of the central Lanzo massif. These peridotites display a pervasive anasto-mosed network of millimetre to centimetre-scale plagioclase-rich bands, which grades locally into a planar layering marked by an intercalation of plagioclase-rich and olivine-rich layers up to tens of centimetres wide. Both the anastomosed and the planar layering are subparallel to the deformation fabric, characterized by a foli-ation defined by the shape-preferred orientation of olivine and by crystal preferred orientation (CPO) of olivine, orthopyroxene, and clinopyroxene. This parallelism, the coexistence of microstructural evidence for melt–rock reactions and for deformation by dislocation creep, and the predominance of axial-[010] olivine CPO patterns, characterized by [010] axes clustered normal to the layering, indicate that deformation and the reactive melt per-colation that formed the layering were coeval. Strong heterogeneity in mineral composition in the planar layering domains, with Fe-enrichment in olivine and spinel and highly variable Ti content in spinel in cm-scale plagioclase-rich bands, implies that the latter interacted with higher melt volumes. High Ti contents in pyroxenes and spinel in the anastomosed layering domains point to changes in melt composition, hinting to less effective melt transport. We propose therefore that the planar layering records melt segregation in layers parallel to the shear plane, whereas the anastomosed layering results from melt alignment along grain boundaries subparallel to the shear plane, without segregation. Finite strain in the different layers cannot be quantified, but comparison of the present observations with data from experiments and from other mantle outcrops displaying shear-controlled melt organization suggests that the transition from the anastomosed to the planar layering might record an increase in finite strain, that is, strain localization associated with variations in the instantaneous melt fraction.

1. Introduction

The mechanical behaviour of partially molten regions in the shallow upper mantle and the processes governing melt transport and distribution in these domains are important, yet largely unresolved questions in geodynamics. Very low melt fractions ($\leq$1%) may reduce the rocks' viscosity by more than one order of magnitude (Rosenberg and Handy, 2000; Takei, 2005). On the other hand, deformation may enhance permeability and lead to melt focussing into layers or channels (Holtzman et al., 2003a,b; Katz et al., 2006). These interactions between melt distribution and deformation play an essential role in localizing strain, as documented in shear zones formed at the lithosphere–asthenosphere boundary (Dijkstra et al., 2002; Kaczmarek and Tommasi, 2011; Kelemen and Dick, 1995; Le Roux et al., 2008) and in the middle and lower crusts (e.g., Brown and Solar, 1998; Hollister and Crawford, 1986; Tommasi et al., 1994).

Experiments showed that deformation of partially molten aggregates in shearing leads to melt segregation into bands oriented at $\leq$20° to the shear plane (Holtzman et al., 2003a, 2005; King et al., 2010; Zimmerman et al., 1999). This melt segregation results in further weakening of the melt–rock aggregates (Holtzman et al., 2012). Melt segregation in layers may also produce anisotropy in viscosity (Holtzman et al., 2012), electrical conductivity (Caricchi et al., 2011), and seismic wave propagation and attenuation in the upper mantle (Holtzman and Kendall, 2010; Vauchez et al., 2000). Shear-induced melt organization has been proposed to strongly contribute to seismic anisotropy in rift zones and, more generally, in the lithosphere–asthenosphere boundary (Holtzman and Kendall, 2010).

A recent study of the shallowmost mantle section (Moho Transition Zone, MTZ) of the Oman ophiolite provided evidence that deformation-controlled melt segregation also occurs in nature and that melt–rock reactions during this process produce compositionally layered peridotites (Higgie and Tommasi, 2012). This study also highlighted a change in olivine crystal preferred orientation from axial-[100] to axial-[010], where the [100] axis becomes distributed in the plane of foliation and [010] concentrated normal to it, in the melt-rich bands. This change

* Corresponding author. Tel.: +33 467144912.
E-mail address: andrea.tommasi@gm.univ-montp2.fr (A. Tommasi).

has been interpreted as due to a combination of melt-assisted glide on preferentially wetted (010) boundaries, local transpressive deformation, and limited activation of the (010)[001] system in olivine (Higgie and Tommasi, 2012). However, these observations come from an end-member situation (active ridge setting, in the vicinity of a mantle diapir), where strong shear deformation affected peridotites containing melt fractions that probably largely exceeded, at least locally, the 1–2% values generally accepted for the upper mantle. One may question if they can be extrapolated to the 'normal' mantle. Here we present a detailed petro-structural study of a section of plagioclase-rich lherzolites from the central domain of the Lanzo peridotite massif in southern Alps, which records interactions with melts at shallow depths in the mantle (<40 km depth; Bodinier et al., 1991).

2. Geological background and study site

The Lanzo massif is a >150 km^2 peridotite body located in the western Alps (Boudier, 1978). It is traditionally interpreted as a part of the mantle section of the Piemont–Ligurian oceanic plate (Lagabrielle et al., 1989), which has been subducted to eclogite facies before fast exhumation during the Alpine orogenesis (Compagnoni and Sandrone, 1979; Kienast and Pognante, 1988). Pervasive eclogitic metamorphic equilibration is however restricted to the borders of the massif (Kienast and Pognante, 1988; Pelletier and Müntener, 2006); most of the massif records a tectono-metamorphic evolution under high-temperature, low pressure conditions interpreted as associated to the extension that formed the Piemont–Ligurian ocean (Bodinier, 1988; Bodinier et al., 1991; Boudier, 1978; Kaczmarek and Muntener, 2008; Lagabrielle et al., 1989).

The massif is split into three bodies: the southern, central and northern bodies (Fig. 1), which are separated by retrogressive shear zones (Boudier, 1978; Kaczmarek and Muntener, 2008; Kaczmarek and Tommasi, 2011). The three bodies have contrasted compositions, which record different evolutions. The northern body is traditionally interpreted as a fragment of subcontinental lithospheric mantle separated from the convective mantle >400 Ma years ago (Bodinier et al., 1991). The southern body was proposed to represent asthenospheric mantle, which rose from the garnet stability field to shallow depths, being submitted to partial melting and melt extraction (6–12%, locally up to 20%) during the formation of the Piemont–Ligurian ocean (Bodinier et al., 1991). The central body, in which the present study area is located, displays transitional geochemical features. It is composed dominantly by plagioclase lherzolites (Boudier, 1978) and was interpreted as a subcontinental mantle lithosphere fragment modified by reactive percolation of low fractions of melts of asthenospheric origin (Bodinier et al., 1991). Reactive transport of MORB-type melts in Central and South Lanzo is recorded in the field by the formation of plagioclase-rich lenses aligned in the foliation or at a low angle to it in the lherzolites, by the development of reactive spinel harzburgite–dunite channels, and by MORB-type gabbro dykes which intrude all lithologies (Bodinier et al., 1991; Boudier, 1978). Reactive melt percolation in Central and South Lanzo is also evidenced by microstructures recording replacement of olivine by orthopyroxene and of clinopyroxene by intergrowths of orthopyroxene and plagioclase (Kaczmarek and Muntener, 2008; Muntener and Piccardo, 2003). Zircon ages in the gabbro dikes date this event at ca. 161–163 Ma (Kaczmarek et al., 2008), whereas the high pressure metamorphism was dated at 45–55 Ma (Rubatto et al., 2008).

Partial melting and reactive melt percolation resulted in an important compositional heterogeneity of the massif, which is illustrated by the variation in Al_2O_3 content of the peridotites (Fig. 1). As the aim of the present study was to analyse the relations between melt and deformation, we focused our observations in the northwestern part of the Central Lanzo body, which shows the highest Al_2O_3 contents within the massif, reflecting high plagioclase contents (Bodinier, 1988). Within this domain, the best outcrops, which were selected for the present study, occur in the Rio Ordagna, between N45°15.56, E7°25.665′ and N45°15.511′, E7°25.324′ (Fig. 1). These outcrops are characterized by coarse-grained peridotites with a well-developed layering recorded by variations in the plagioclase content (Fig. 2).

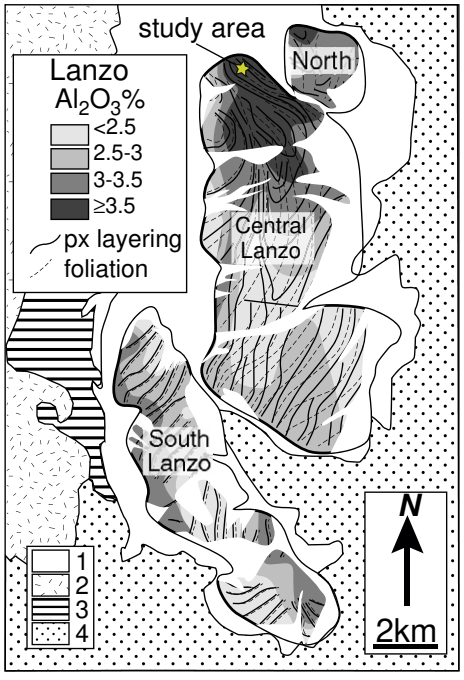

Fig. 1. Simplified map of the Lanzo peridotite displaying the location of the study area in the northwestern part of the Central Lanzo body, which shows the highest Al_2O_3 contents within the massif, reflecting high plagioclase fractions. Al_2O_3 content map and foliation and pyroxenite layering orientations were derived from Bodinier (1988) and Boudier (1978), respectively. (1) Lanzo serpentinite; (2) Piedmontese ophiolitic sequences; (3) Mesozoic metasedimentary rocks; (4) Late cenozoic metasedimentary rocks.

3. Methods

Twenty-one 25 mm-wide geographically oriented cores sampling the different compositional and textural facies observed in a 500 m long almost continuous riverbed outcrop were drilled in three locations separated by ~50 m (Table 1). Due to the necessity to drill on a flat surface, the cores were often drilled oblique to the compositional layering. To sample the textural variability at the cm-scale and to ensure that a representative volume was analysed, for most cores, two polished thin-sections for microstructural analysis and crystal preferred orientation (CPO) measurements were prepared along a vertical plane containing the core axis. Core orientations were used to rotate the crystal preferred orientation data to a geographic reference frame using the Rotctf programme by D. Mainprice (ftp://www.gm.univ-montp2.fr/mainprice//CareWare_Unicef_Programs/). This rotation allowed straightforward comparison between the CPO data from different samples and between the CPO and the orientation of the layering.

CPO of olivine, orthopyroxene, clinopyroxene, and plagioclase were measured by indexation of electron back-scattered diffraction (EBSD) patterns at the Geosciences Montpellier SEM-EBSD facility using a scanning electron microscope JEOL JSM5600 with an acceleration voltage of 17 kV and a working distance of 23 mm. Oxford Instruments Channel + software was used to process the images and index the minerals with respect to their crystallographic orientation. Orientation maps covering 80–90% of the thin section surface were acquired in automatic acquisition mode. Step sizes between 35 μm and 80 μm were used (at least 1/4 of the smallest grain size) to ensure a correct sampling of the smaller grains. Raw indexation rates ranged from 45% to 80%. Non-indexed areas resulted from polishing defects, alteration, fractures,

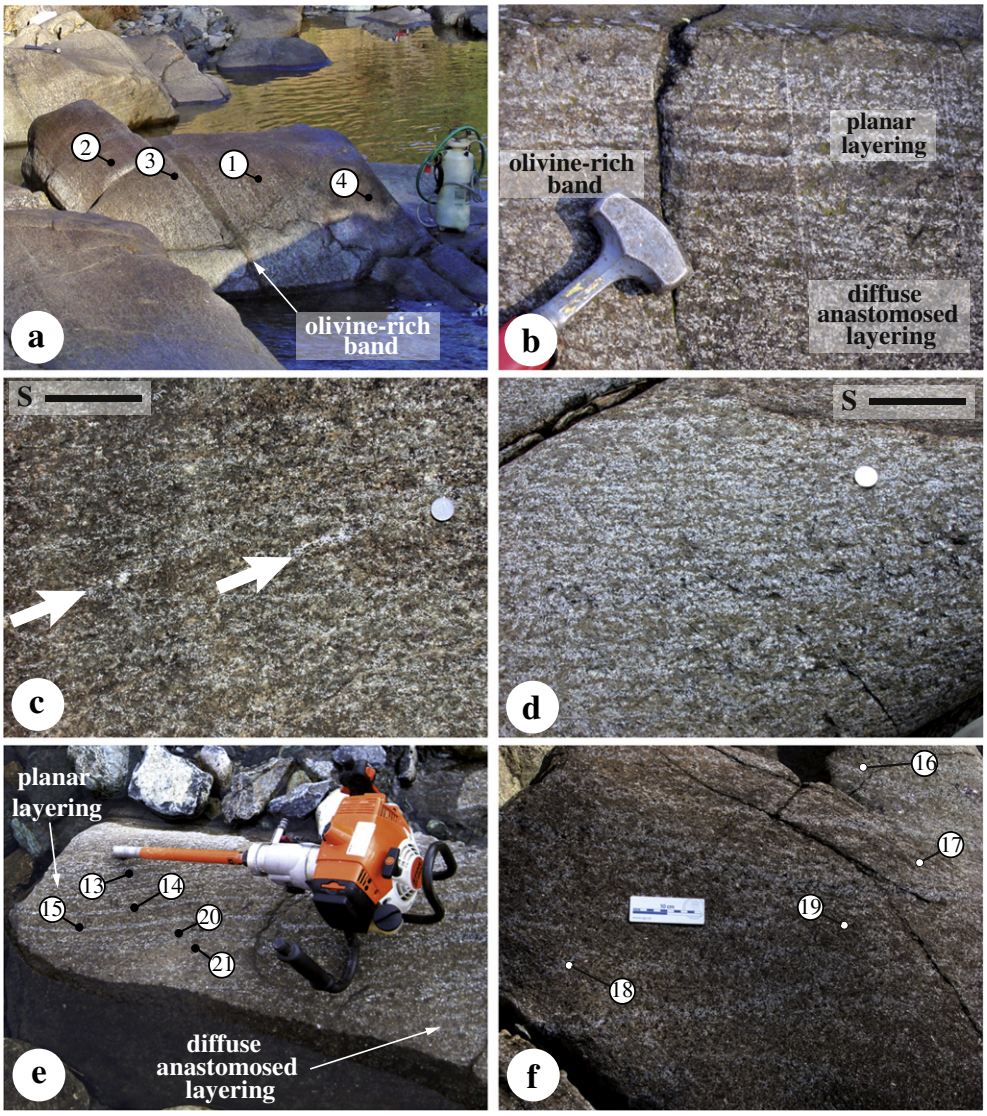

Fig. 2. Meso and macroscopic structures. (a) Dominant diffuse anastomosed layering that grades to a planar layering containing a ~10 cm thick olivine-rich layer in the centre of the photo; labels mark the location of cores 1 to 4, which sample the diffuse anastomosed layering. (b) Detail of the transition between the diffuse anastomosed layering to the planar layering domain. (c) Diffuse anastomosed layering, white arrows mark plagioclase concentrations oblique (~20° counterclockwise) to the dominant orientation of the layering (S), indicated by the black line. (d) Plagioclase-rich section within the diffuse anastomosed layering. (e) Planar layering domain, which grades at the bottom of the photo into a coarse anastomosed layering; labels mark the location of cores 13 to 15 and 20 to 21, which sample planar layers with different plagioclase contents and the transition between a planar and a coarse anastomosed layering, respectively. (f) Coarse anastomosed layering, characterized by cm-thick diffuse plagioclase-rich layers enclosing olivine-rich lenses a few cm thick and tens of cm long (continuation of outcrop displayed in (e)); labels mark the location of cores 16 to 19.

and grain boundaries. Standard post-acquisition data treatment for olivine-rich rocks (cf. Tommasi et al., 2008), controlled by comparison with optical microscopy observations, allowed the increasing of the proportion of indexed points. All CPOs are shown on equal area lower hemisphere stereonets in the geographic reference frame. They are plotted as one average orientation measurement per grain to avoid oversampling of larger crystals and are density contoured when more than 100 grains could be measured in the thin section.

CPO intensities and symmetry were analysed using both one-orientation-data-per-pixel and one-average-orientation-per-grain, ensuring in the latter case that ≥100 grains were measured to ensure statistical representativity (Ben Ismail and Mainprice, 1998). The CPO strength was determined using the J-index, which is the volume-averaged integral of the squared orientation densities, ranging from 1 for a random distribution to infinity for a single crystal (Bunge, 1982). The J-index was calculated using the MTEX toolbox in MATLAB (Bachmann et al., 2010; Hielscher and Schaeben, 2008; Mainprice et al., 2011), using orientation distribution functions (ODF) calculated using a 'de la Vallée Poussin' kernel with a half width of 10°, corresponding to a bandwidth of 28.

To characterize the symmetry of the olivine CPO the BA-index was used. This index is based on the LS-index proposed by Ulrich and Mainprice (2005). It is calculated as:

$$\text{BA\_index} = 1/2\left(2-\left(\frac{P_{010}}{G_{010}-P_{010}}\right)-\left(\frac{G_{100}}{G_{100}-P_{100}}\right)\right) \quad (1)$$

where P and G are the Point and Girdle fabric indices (Vollmer, 1990) for the [100] and [010] crystallographic axes. These indices are calculated using the MTEX software (Bachmann et al., 2010; Hielscher and Schaeben, 2008). For each axis, the orientation tensor and its three eigenvalues $\lambda_1, \lambda_2, \lambda_3$(where $\lambda_1 \geq \lambda_2 \geq \lambda_3$ and $\lambda_1 + \lambda_2 + \lambda_3 = 1$) are used to determine:

$$P = \lambda_1 - \lambda_2 \text{ and } G = 2(\lambda_2 - \lambda_3). \quad (2)$$

Table 1
Sample description and olivine CPO data (J- and BA-indexes). Starred samples had two parallel thin sections produced from the same core (modes and CPO data are averaged over the two sections). Italicized samples are those selected for EMPA analysis of mineral compositions. Plg = plagioclase; SPO = shape-preferred orientation.

Sample	Layering	Modal composition (%)					Olivine CPO		Description
		Ol	Opx	Cpx	Plg	Sp	J	BA	
KHLZ1*	016/60SE	64.5	19	9	.5	1	6.16	0.43	Anastomosed layering: plg-rich domain with distributed isolated plg crystals and plg-poor domain containing 2 mm wide plg-rich lenses
KHLZ2	016/60SE	67	13	11	9	–	7.67	0.35	Anastomosed layering: mostly plg-poor, but containing discontinuous 2–3 mm wide plg-rich layers
KHLZ3	016/60SE	61	17	11	1	–	3.9	0.44	Anastomosed layering: 1–3 mm wide plg-rich layers enclose plg-poor lenses (~6 mm wide and 15 mm long), large 'poikilitic' opx
KHLZ4	040/50SE	70	13	9	8	–	5.16	0.37	Anastomosed layering: plg-rich lenses, very altered
KHLZ5	040/50SE	79	13	4	3	1	6.78	0.46	Planar layering: olivine-rich, plg-poor layer a few cm wide, in between 6 & 7, olivine SPO
*KHLZ6**	040/50SE	66.5	13	9	11	0.5	4.57	0.44	Planar layering: plg-rich layer 1–2 cm wide, core at low angle to layering plane, plg evenly distributed, forming lenses slightly elongated parallel to olivine lineation
KHLZ7*	040/50SE	72	9	10	9	–	4.75	0.43	Transition from planar to anastomosed layering: mostly plg-poor, but containing discontinuous plg-rich layers 2–3 mm wide, weak olivine SPO, sp elongated
*KHLZ8**	050/50SE	68	15	10	7	–	7.34	0.20	1 m thick band with diffuse anastomosed layering: interconnected plg-rich lenses, very coarse grains
KHLZ9*	050/50SE	67	15	11	7	–	6.2	0.18	Anastomosed layering: large plg-poor lenses containing isolated interstitial plg surrounded by discontinuous plg-rich layers
KHLZ10*	050/50SE	64	18	9	8	1	4.59	0.32	Anastomosed layering: large plg-poor lenses containing isolated interstitial plg surrounded by discontinuous plg-rich layers
KHLZ11	050/50SE	69	19	6	6	–	6.44	0.37	Limit between a planar and an anastomosed layering domain: discontinuous plg-rich lenses parallel to olivine SPO
KHLZ12*	050/50SE	71.5	16	9	3	0.5	4.62	0.22	Anastomosed layering: plg-poor layer with distributed interstitial plg in the lower part
KHLZ13	030/50SE	88	5	3	4	–	5.49	0.35	Planar layering: plg-poor with discontinuous 2–3 mm wide plg-rich lenses in the upper part of the thin section, weak olivine SPO
KHLZ14	030/50SE	76	10	3	10	1	5.39	0.41	Planar layering: well-defined 1–2 cm wide plg-rich layer, very coarse grain size (>1 cm) in olivine-rich layer
*KHLZ15**	030/50SE	79	2	11	8	–	5.0	0.37	Planar layering: well-defined 1 cm wide plg-rich layers
KHLZ16*	030/50SE	70	17	7	6	–	4.62	0.31	Transition between anastomosed and planar layering: dominantly anastomosed, 2–3 mm wide diffuse plg-rich layers surrounding ol-rich lenses
KHLZ17*	060/40SE	71	22	3	4	–	7.45	0.31	Transition between anastomosed and planar layering: mainly plg-poor, but diffuse plg-rich layers in the upper part of thin section
*KHLZ18**	060/40SE	72.5	14	6	7	0.5	5.24	0.28	Coarse anastomosed layering: 2–5 mm wide continuous plg-rich layers enclosing cm-scale plg-poor lenses containing some interstitial plg
KHLZ19*	060/40SE	68	21	7	4	–	5.46	0.35	Coarse anastomosed layering: plg-poor lens containing aligned plg-rich aggregates, very coarse grain sizes (up to 1 cm)
KHLZ20*	060/40SE	81	8	4	7	–	5.8	0.29	Transition between coarse anastomosed and planar layering: irregularly shaped plg-rich lenses
KHLZ21*	060/40SE	76	13	6	5	–	5.75	0.28	Transition between coarse anastomosed and planar layering: discontinuous plg-rich layers

For a perfect axial-[010] CPO (also called fibre-[010]), the P and G values for [010] and [100] are 1, 0 and 0, 1, respectively, and the BA-index is 0. For a perfect axial-[100] CPO (also called fibre-[100]), the P and G values for [100] and [010] are 1, 0 and 0, 1, respectively, and the BA-index is 1.

Modal compositions were estimated from EBSD maps. Due to widespread alteration, plagioclase was poorly indexed, except in sample 9, where it was fresh. The modal percentage of plagioclase was thus estimated by manual drawing of the plagioclase distribution in plane-polarized and cross-polarized optical images of the thin sections and treating the resulting image with Photoshop and ImageJ.

Mineral compositions in eight thin sections representative of the different lithologies and textures were analysed at Université Montpellier 2 using a CAMECA SX100 Electron Probe Micro Analyser (EPMA) equipped with five wavelength-dispersive X-ray spectrometers (WDS) using an accelerating voltage of 20 kV, a beam current of 10 nA, and 30 s counting time for all elements.

4. Results

4.1. Field observations: meso- and macroscale structures

The studied section is mainly composed of plagioclase and spinel-bearing lherzolites, which display a well-developed compositional layering marked in the field by variations in the plagioclase (and pyroxene) content (Fig. 2a–f). The morphology of the layering varies at the decimetre (Fig. 2a,b) to tens of metres scale.

A pervasive anastomosed network of plagioclase-rich bands with diffuse limits, a few millimetres to centimetre wide, enclosing plagioclase-poor lenses, characterizes most of the section (Fig. 2a–d, f). The anastomosed nature of the layering results from orientation of the plagioclase-rich lenses both parallel (dominant) and at ~20° to the peridotite foliation (arrows in Fig. 2c). The relative proportion of plagioclase-rich bands and plagioclase-poor lenses is highly variable. Plagioclase-rich domains contain olivine-rich lenses a few millimetres wide and 1–2 cm long (Fig. 2d), whereas in plagioclase-poor domains, diffuse millimetre-thick plagioclase bands surround olivine-rich lenses few centimetres wide and tens of centimetres long (Fig. 2f). Outcrops parallel to the layering do not show a clear shape-preferred orientation of the plagioclase-rich bands or plagioclase-poor lenses indicating a planar (oblate) fabric. In addition, plagioclase-rich domains tend to have a more planar structure than the plagioclase-poor ones (compare Fig. 2d and c,f).

This anastomosed compositional layering locally grades into a planar banding formed by the alternation of layers a few millimetres to tens of centimetres wide, which are strongly enriched or depleted in plagioclase (Fig. 2a, b, and e). Olivine-rich layers are, in average, thicker than plagioclase-rich ones (Fig. 2b and e). These layers have diffuse limits (Fig. 2b) and are rather continuous in length; some may be followed for a few metres. Rare, metric-scale spinel-bearing dunitic layers also occur in the studied section. In these thick dunitic layers, the spinel displays whitish rims, which could be interpreted as plagioclase rims, but are mainly due to alteration to chlorite. 1–10 cm wide pyroxenite bands, generally concordant with the plagioclase layering, also occur locally.

The changes in the layering morphology from anastomosed to planar or in the relative content in olivine and plagioclase do not follow a regular pattern. They are repeated many times over the studied section, which is composed by discontinuous metric to decametric scale outcrops spread over ~200 m along the riverbed. There is also no evidence of modal grading, i.e., plagioclase contents or the frequency of plagioclase-rich bands becoming more/less frequent up or down

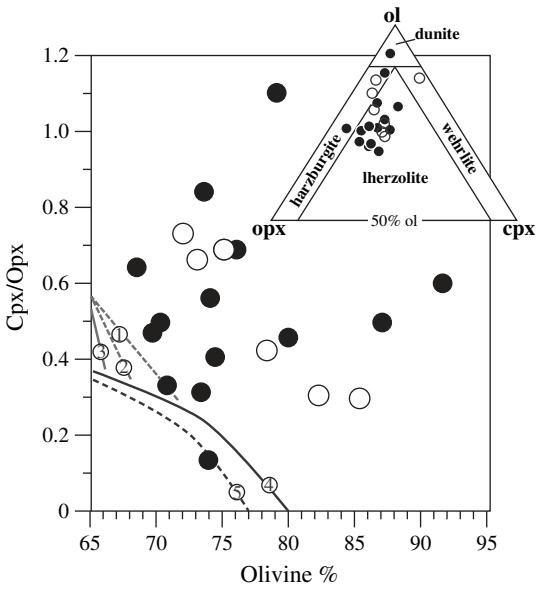

Fig. 3. Modal compositions. Olivine content vs. clinopyroxene/orthopyroxene ratio, normalized to 100% for comparing with isobaric (grey lines: 1 = 11 kb, 2 = 16 kb, 3 = 17 kb) and polybaric (black lines: 4 = excess olivine; 5 = no excess olivine) melting models (Niu et al., 1997; Walter et al., 1995). The white circles indicate the samples selected for analysis of mineral compositions. Insert displays the olivine (ol)–orthopyroxene (opx)–clinopyroxene (cpx) ternary diagram projected from the plagioclase pole.

section. Despite the variations in morphology, the layering orientation remains constant, with a NE direction (20–60°) and intermediate dips (40–60°) towards the SE over the entire studied section.

4.2. Modal compositions and microstructures

Most cores sampled the dominant diffuse anastomosed layering, but cores 5, 6, 13, 14, and 15 sampled the planar layering (Table 1). Most samples are fertile plagioclase lherzolites (Fig. 3, Table 1). When averaged at the thin section scale, plagioclase content ranges from <3% to 11% (Table 1). However, the plagioclase distribution is highly heterogeneous (Fig. 4); at least half of the analysed thin sections display plagioclase-poor regions (<2% plg) that alternate with plagioclase-rich lenses or layers; the latter may be up to 1 cm wide and have plagioclase contents of ~30% (Fig. 4d).

All samples display coarse-grained porphyroclastic to coarse granular textures (Fig. 4). Olivine and orthopyroxene crystals may reach >1 cm in diameter (Fig. 4d, upper left corner). The grain size distribution is, however, not bimodal; grain sizes vary continuously. Olivine crystals have irregular shapes, with interpenetrating grain boundaries, but display a weak shape preferred orientation, marking the foliation (Figs. 4 and 5a). Small polygonal crystals, as well as locally straight grain boundaries and triple junctions are also common (Fig. 5b). Although rare, 90° four-grain junctions were also observed. Undulose extinction and subgrain boundaries are ubiquitous (Figs. 4 and 5a,b). Olivine often displays concave contacts with orthopyroxene or occurs as inclusions in the latter (Fig. 5c–e).

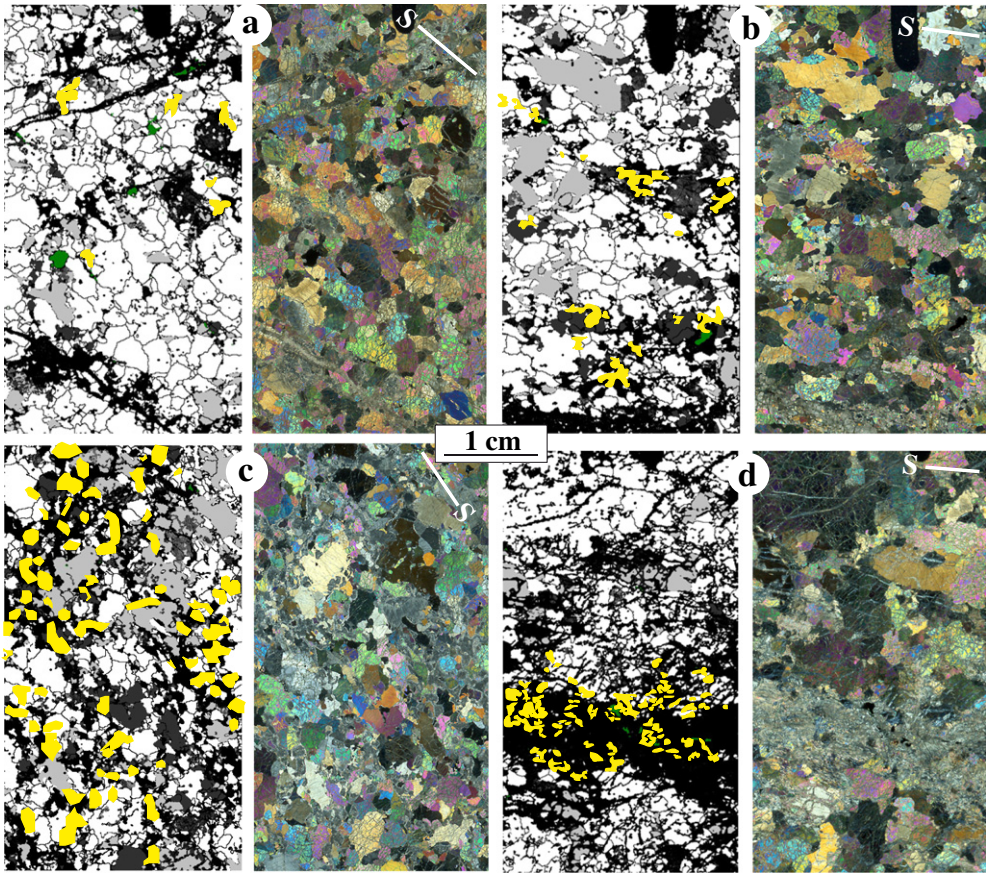

Fig. 4. Mineral composition maps derived from EBSD data (white = olivine, light grey = orthopyroxene, dark grey = clinopyroxene, green = spinel, and black = non-indexed areas), with the plagioclase distribution highlighted in yellow and microstructures (photomicrographs under crossed polarized light) for four typical thin sections. (a) Plagioclase-poor layer from a planar layering domain (sample 5). (b) Discontinuous mm-scale plagioclase-rich layers from a diffuse anastomosed layering domain (sample 9B). (c) Diffuse anastomosed layering domain, plagioclase-rich layer (sample 3). (d) Alternating centimetre-scale plagioclase-poor and plagioclase-rich layers in the planar layering domain (sample 14).

Orthopyroxene generally occurs as large (up to 15 mm wide), irregularly shaped grains with sinuous grain boundaries (Figs. 4b upper left corner and 5c–e), which form cusps 'filling' triple junctions with olivine grains (Fig. 5c–d) or even enclose fragments of a previously unique olivine crystal, as indicated by their common extinction angle (Fig. 5c). Large orthopyroxene crystals often have olivine inclusions, which have an almost identical orientation to adjoining olivine crystals (Fig. 5d). Orthopyroxene shows no obvious shape preferred orientation, but undulose extinctions and kinks are common (Fig. 5d–e). Fine exsolution lamellae of clinopyroxene are ubiquitous (Fig. 5c–e). In the plagioclase-rich lenses, orthopyroxene is often associated with plagioclase (Fig. 5f,h).

Clinopyroxene often occurs as irregularly shaped grains with cusped grain boundaries (Fig. 5f). It has generally smaller grain sizes than orthopyroxene (<8 mm). It often contains orthopyroxene exsolution lamellae (Fig. 5c) and may also contain olivine inclusions. Some crystals, but not all, show undulose extinction.

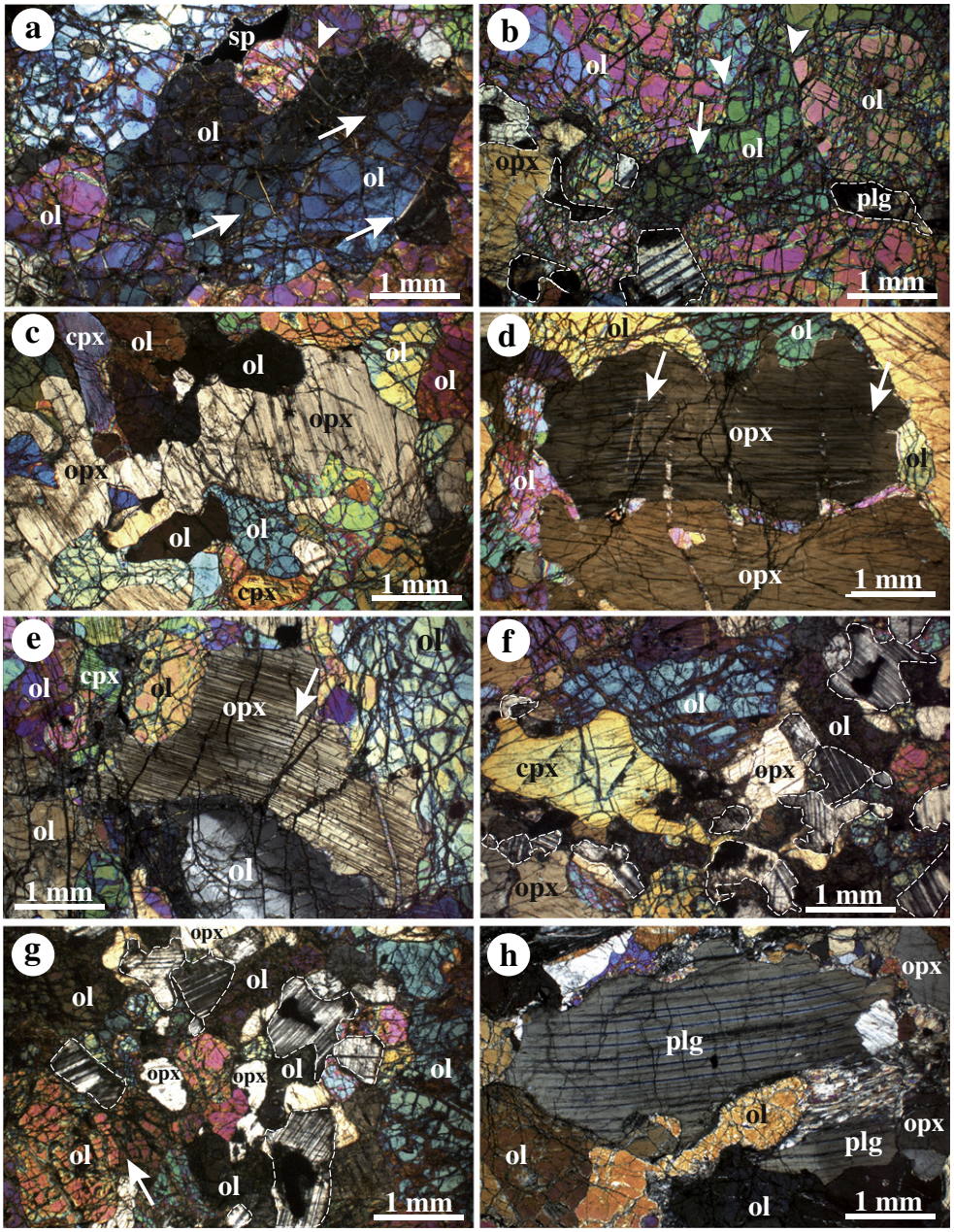

Fig. 5. Photomicrographs in plane-polarized light illustrating typical microstructures. (a) Irregularly shaped olivine crystals, with interpenetrating grain boundaries, undulose extinction, and subgrains (long white arrows mark subgrain boundaries, short white arrows indicate 120° triple junctions). (b) Olivine crystals with more polygonal shapes (arrows as in (a)) intercalated with small plagioclase crystals (outlined by thin white dashed lines) with either subhedral shapes and mechanical twins or irregular shapes. (c) Irregularly-shaped orthopyroxene, with interpenetrating grain boundaries with olivine; note that this orthopyroxene separates fragments of olivine crystals with similar crystal orientations, denoted by the similar birefringence. (d & e) Large irregularly-shaped orthopyroxene crystals with interpenetrating grain boundaries with olivine and kinks (white arrow) marked by the sharp change in the orientation of the clinopyroxene exsolutions. (f) Detail of a diffuse plagioclase-rich layer showing the irregular shapes of the individual plagioclase crystals (outlined by thin white dashed lines) and their association with ortho- and clinopyroxene; note the very irregular shape of clinopyroxene and the spinel cores in some plagioclases. (g) Plagioclase and orthopyroxene-rich lens in an olivine-rich domain, plagioclase crystals show either subhedral or irregular shapes, mechanical twins, and sometimes spinel cores, orthopyroxene has interstitial shapes (white arrow marks a subgrain wall in olivine). (h) Rare large isolated plagioclase crystal elongated parallel to the foliation, but with irregular grain boundaries, displaying bending of the crystalline network outlined by the twins.

Plagioclase is often completely transformed to sericite, but the aggregates preserve their original shape (Fig. 4). Although they were not observed optically in the studied thin sections, very small volumes of relict high-pressure assemblages (zoizite ± talc ± kyanite ± chloritoid) as the ones described in metagabbros crosscutting the peridotites in this part of the massif (Pelletier and Müntener, 2006), may also be present in these aggregates. For simplicity sake, in the following, although strongly transformed during the late stages of the evolution of the massif, these aggregates will be referred to as plagioclase. In layers with low plagioclase contents, the plagioclase occurs as isolated crystals with irregular shapes, forming discontinuous chains aligned in the foliation (Figs. 4a, 5b). Most often, plagioclase occurs in lens-shaped aggregates a few mm wide and a few cm long (Fig. 4b) or in discontinuous layers ranging from a few mm wide (Fig. 4c) to 1–2 cm wide (Fig. 4d). These plagioclase-rich lenses or layers are composed of plagioclase, pyroxenes, and olivine. Plagioclase crystals have usually irregular, interstitial shapes (Fig. 5b,f–h), but may locally be subhedral (Fig. 5b,g). They are usually 1–2 mm long, but may attain 5 mm (Fig. 5h). Plagioclase crystals have undulose extinction and mechanical twins (Fig. 5b,f–h). Some crystals display spinel cores (Fig. 5f,h).

Spinel occurs most often as isolated submillimetric crystals with irregular, holy-leaf shapes (Fig. 5a), which may show chlorite rims. It may display a shape-preferred orientation or crystal alignments that mark the lineation.

4.3. Crystal preferred orientation (CPO)

Fig. 6 illustrates the olivine, orthopyroxene, and clinopyroxene CPO in 5 cores characterized by different plagioclase contents. The CPO data for all cores is presented in the Supplementary material (Fig. S1).

Olivine displays a clear CPO, which is coherent with the field-measured compositional layering (Fig. 6). A small (<5°) anticlockwise rotation between the olivine CPO and the compositional layering is, however, observed in some samples (cf. sample 12 in Fig. 6). The CPO symmetry ranges from orthorhombic to axial-[010], with a predominance of axial-[010] patterns (BA-indexes < 0.35, Fig. 7a). In both cases, [010] axes cluster normal to the layering and [100] and [001] axes are distributed in a girdle along the layering plane, forming two roughly orthogonal maxima, which are usually weaker to the [010] one and of equivalent intensity (Fig. 6).

The olivine CPO is rather strong, with J-indexes ranging from 4 to 8 (Fig. 7). There is no clear correlation between the olivine CPO strength or symmetry and the olivine content when the analysis is performed at the core scale (addition of data acquired on the two thin sections parallel to the core axis, when possible), but the compositional variations occur at the cm scale and most cores are composed by layers with very different plagioclase contents. A fine analysis of the changes in olivine CPO symmetry and intensity at the layers' scale could not be performed, because the compositional layering is in most cases only a few

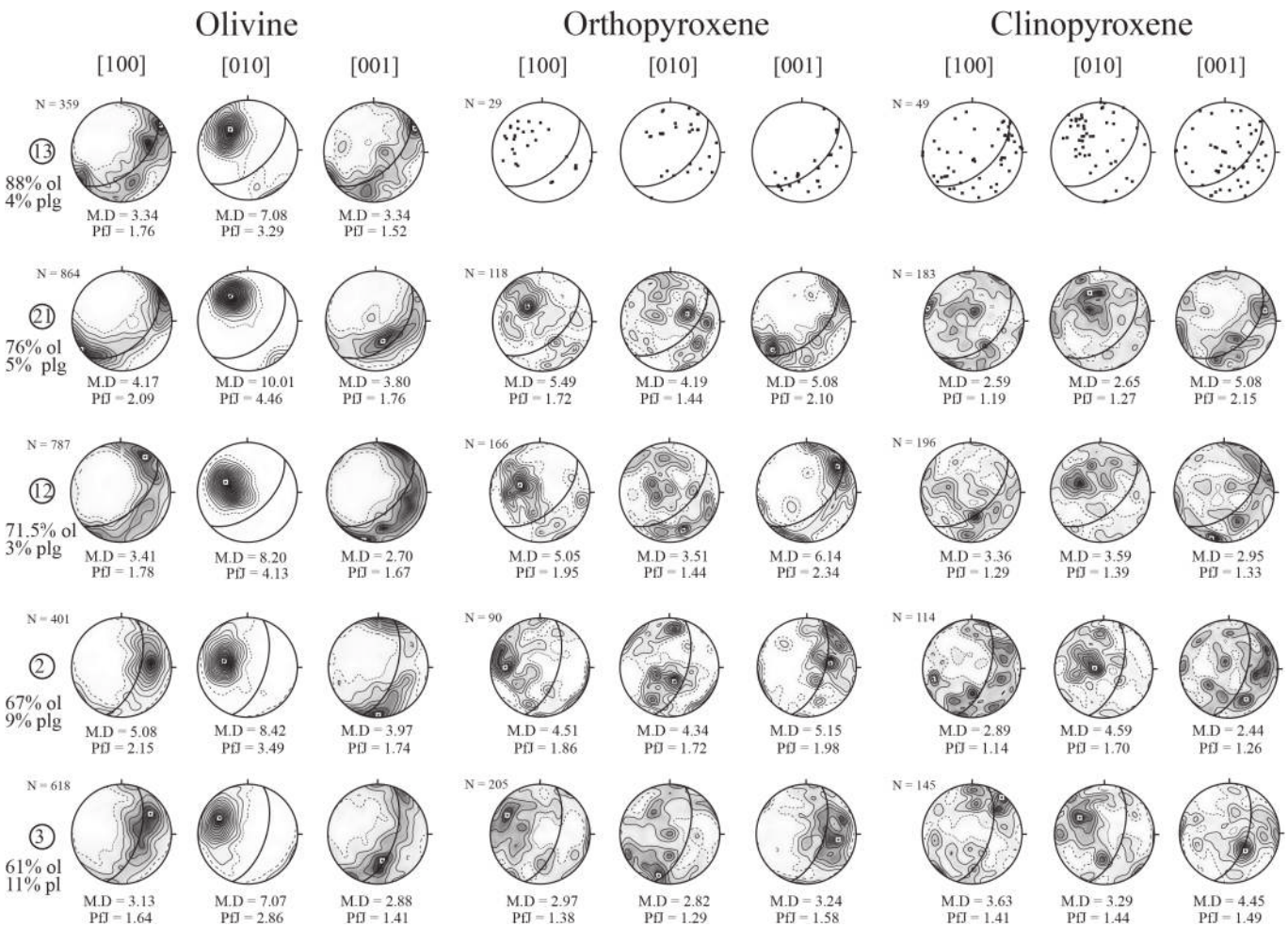

Fig. 6. Pole figures showing typical relations between the crystal preferred orientations (CPOs) of olivine, ortho- and clinopyroxene for representative samples with variable plagioclase contents and different morphologies of the layering (2, 3, and 12 = diffuse anastomosed layering; 13 = planar layering; 21 = transition between diffuse anastomosed and planar layering, cf. Table 1). Lower hemisphere stereoplots in the geographic reference frame, North at the top and East on the right; contours at 0.5 multiples of a uniform distribution (m.u.d.); when less than 90 grains were measured, stereoplots were not contoured. MD = maximum density of the contours. The solid line represents the compositional layering.

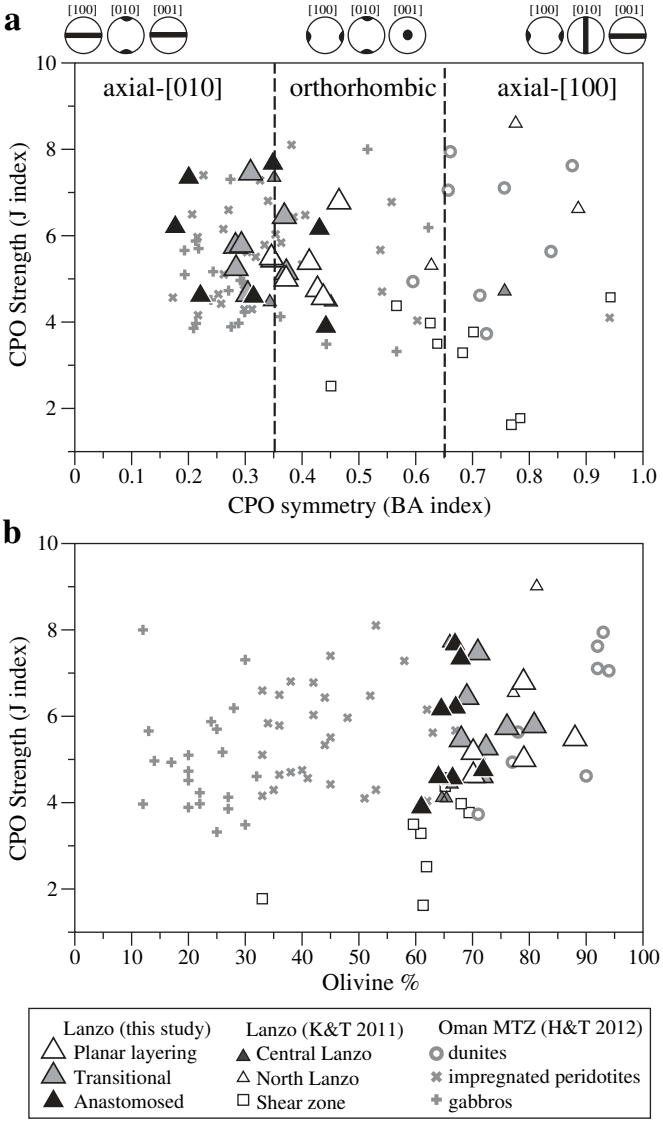

Fig. 7. Strength of the olivine CPO, quantified by the J-index, vs (a) the symmetry of the olivine CPO, quantified by the BA-Index, and (b) the modal content of olivine as a function of the layering morphology (planar, anastomosed, or transitional, cf. Table 1). In the planar layering domains, olivine CPO could only be measured in the olivine-rich layers due the high alteration degree of the plagioclase-rich layers. Cartoons in (a) describe the typical CPO for two end-member cases for the BA index (BA = 0, axial-[010] CPO and BA = 1, axial-[100] CPO). In both diagrams, published data from the Oman MTZ (Higgie and Tommasi, 2012) and from peridotites from northern Lanzo shear zone (Kaczmarek and Tommasi, 2011) are shown for comparison.

grains (3–10) wide and, as a consequence, not enough olivine grains could be measured within a homogeneous compositional layer. Nevertheless, samples from planar layering domains, in which the olivine CPO is dominated by data from the plagioclase-poor layers, show systematically orthorhombic olivine CPO (BA-indexes > 0.35, Fig. 7a). Samples from domains transitional between anastomosed and planar layering show olivine CPO with symmetries intermediate between axial-[010] and orthorhombic (0.25 < BA-index < 0.38). In contrast, anastomosed layering samples have highly variable olivine CPO symmetry, ranging from strongly axial-[010] (BA-index = 0.18) to orthorhombic (BA-index = 0.44).

Orthopyroxene has also a clear CPO, characterized by an alignment of [001] axes in the layering plane with a maximum that is subparallel to the olivine [100] axes maximum (Fig. 6). [100] axes tend to concentrate at high angle to the layering. [010] axes are more dispersed. Clinopyroxene shows a much weaker CPO (Fig. 6). In most cores, [001] axes form, however, a wide girdle in the layering plane, with a poorly-defined maximum parallel to the orthopyroxene [001] maximum, and [010] axes tend to concentrate normal to the layering. [100] axes are very dispersed, but tend to align in the layering plane.

Due to pervasive alteration, a statistically significant plagioclase CPO could only be measured in core 9, which contains ~7% of plagioclase, mostly concentrated in anastomosed bands 3–5 mm wide, but also as isolated crystals in the olivine-rich lenses. Plagioclase shows a clear crystal preferred orientation (Fig. 8), which is correlated with the olivine CPO. The plagioclase [100], [010], and [001] maxima are close to the [100], [010], and [001] maxima of olivine, respectively. However, plagioclase [100] and [001] axes tend to show point-like concentrations, whereas the olivine [100] and [001] axes are dispersed in the layering plane. Moreover, there is a 15° anticlockwise rotation of the plagioclase CPO relative to both the compositional layering and the olivine CPO.

4.4. Mineral compositions

Eight samples from 7 cores were chosen for EMPA analysis based on their differing plagioclase contents and distributions to check for heterogeneities in the mineral chemistry that could record spatial variations in melt content. We focused therefore on gradients in the mineral composition that may be directly associated to reactive melt percolation, such as enrichment in Fe in olivine, pyroxenes, and spinel or in Ti in pyroxenes and spinel. Sub-solidus re-equilibration in both cases will result in the smoothing of the chemical gradients; it may therefore partially mask the effect of a heterogeneous melt percolation. The analysed samples are highlighted in Table 1 and their mineral compositions are shown in Supplementary material Table S1.

Plagioclase has a labradorite composition, with higher An contents in the rims (76–77) than in the cores (67–72). Ti contents vary between 125 and 400 ppm and Cr contents are <60 ppm.

Olivine Mg# ranges from 86 to 90. Systematic core–rim variations were not observed, but the lowest values (Mg# < 88) were measured in olivine crystals within or close to plagioclase-rich layers in samples derived from planar layering or coarse anastomosed layering domains

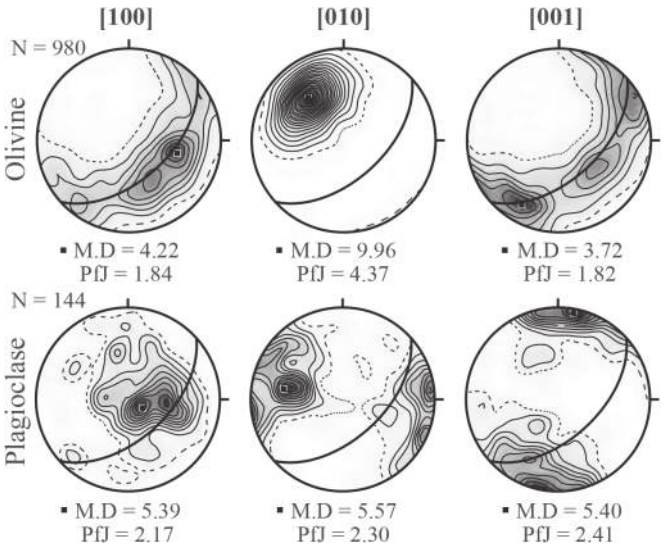

Fig. 8. Plagioclase and olivine CPOs in sample 9 (measurements on two parallel thin sections along the core axis). Lower hemisphere stereoplots in the geographic reference frame, North at the top and East on the right; contours at 0.5 multiples of a uniform distribution (m.u.d.). MD = maximum density of the contours. The solid line represents the compositional layering.

(samples 14, 15, and 18B in Fig. 9a). These samples also show the largest variation in olivine Mg#, encompassing the whole range of analysed values, as olivine crystals in plagioclase-poor layers in these samples have 'normal' mantle compositions (Mg# ≥ 89). The highest and least variable olivine Mg# (89–89.5) is displayed by a plagioclase-poor lens in an anastomosed layering domain (sample 9A in Fig. 9a). Intermediate olivine Mg# (88–89.2) is observed in samples from anastomosed layering domains showing plagioclase-rich layers (samples 6A and 8B in Fig. 9a) and by an olivine-rich layer from a planar layering domain (sample 5 in Fig. 9a). Ni contents in olivine vary from 2250 ppm to 3310 ppm. High and least variable Ni contents are observed in plagioclase-poor sample 9, but the other samples show no correlation between the Ni content and olivine Mg# (Fig. 9a).

Orthopyroxenes are enstatites with Mg# between 88.5 and 90.2 and Ti contents from 500 to 2400 ppm (Fig. 9b and Table S1). Orthopyroxenes from diffuse anastomosed layering domains show high Ti contents (≥1500 ppm), but variable Mg#, which are lower in the plagioclase-poor layers (Mg# ≥ 89.5) than the plagioclase-rich ones (Mg# = 88.5–89.3). Orthopyroxenes from planar layering domains show in average lower Ti contents (<1500 ppm). In addition, orthopyroxenes from plagioclase-rich layers in planar layering domains have higher Mg# (>89.7) than those from the plagioclase-poor layer.

Clinopyroxenes are augites rich in Al_2O_3 (Table S1). They have highly variable Mg# (88–92) and Ti contents (1500–6000 ppm, Fig. 9c). Few rims were measured but they tend to have slightly higher Mg# and Ti contents. Mg# and Ti contents in clinopyroxenes are correlated to those in orthopyroxene. Clinopyroxenes from planar layering domains have low Ti contents (<4000 ppm): the plagioclase-poor sample (5) has the clinopyroxenes with the lowest Mg# (88.3) and Ti contents (<2500 ppm), whereas samples with both plagioclase-poor and plagioclase-rich layers have clinopyroxenes with high Mg# (>89.5) and intermediate Ti contents (2000–4000 ppm). Clinopyroxenes from diffuse anastomosed layering domains have higher Ti contents (>4000 ppm); their Mg# are more heterogeneous and, in average, lower in the plagioclase-rich layers or lenses.

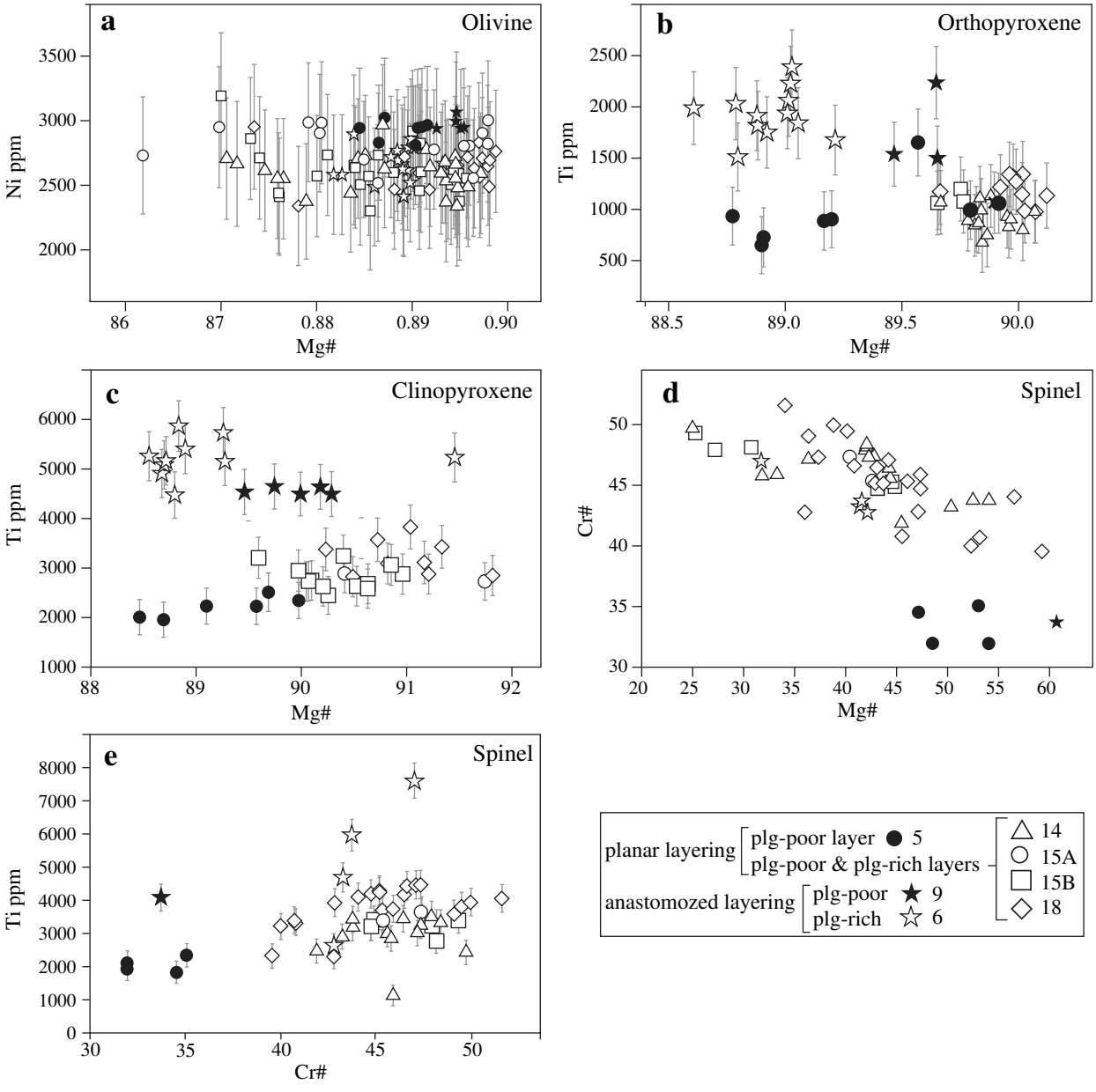

Fig. 9. Mineral composition data. (a) Olivine Mg# vs. Ni content in ppm. (b) Orthopyroxene Mg# vs Ti content in ppm. (c) Clinopyroxene Mg# vs Ti content in ppm. (d) Spinel Mg# vs. Cr#. (e) Spinel Cr# vs. Ti content in ppm. 1σ error bars are displayed for Ni, Cr, and Ti.

The spinel composition varies widely (Fig. 9d–e, Table S1). Plagioclase-poor layers have spinels with low Cr# (32–36), high Mg# (45–65), and high Ni contents (1800–2000 ppm). Ti contents in spinel from plagioclase-poor layers are low in planar layering domains, but intermediate (~4000 ppm) in diffuse anastomosed layering domains. Plagioclase-rich layers have spinels with higher Cr# (39–52), which shows a weak negative correlation to the Mg# (25–60). The samples with well-developed cm-scale plagioclase-rich bands (14A, 15A–B, and 18) show almost as much variation in both Cr# and Mg# within a thin section as in the entire dataset. In these samples, spinel with lower Mg# is generally associated with the plagioclase-rich bands. The Ti content in plagioclase is also highly variable (1000–8000 ppm); the highest values are observed in spinels from plagioclase-rich layers or lenses in diffuse anastomosed layering domains.

The relations between the layering structure and the mineral chemistry data are illustrated in Fig. 10, which presents mineral compositions as a function of the location of the analysis point and the plagioclase distribution for a plagioclase-poor and three layered thin sections. Although the relation is not one to one, in plagioclase-poor sample 9A olivine has always high Mg# and Ni contents, whereas olivine crystals within or in the vicinity of the cm-wide plagioclase-rich bands in the planar layering domains have mainly low Mg# (<88). The cm-wide plagioclase-rich layers in planar layering domains are also characterized by clinopyroxenes with lower Ti contents and spinels with lower Mg#.

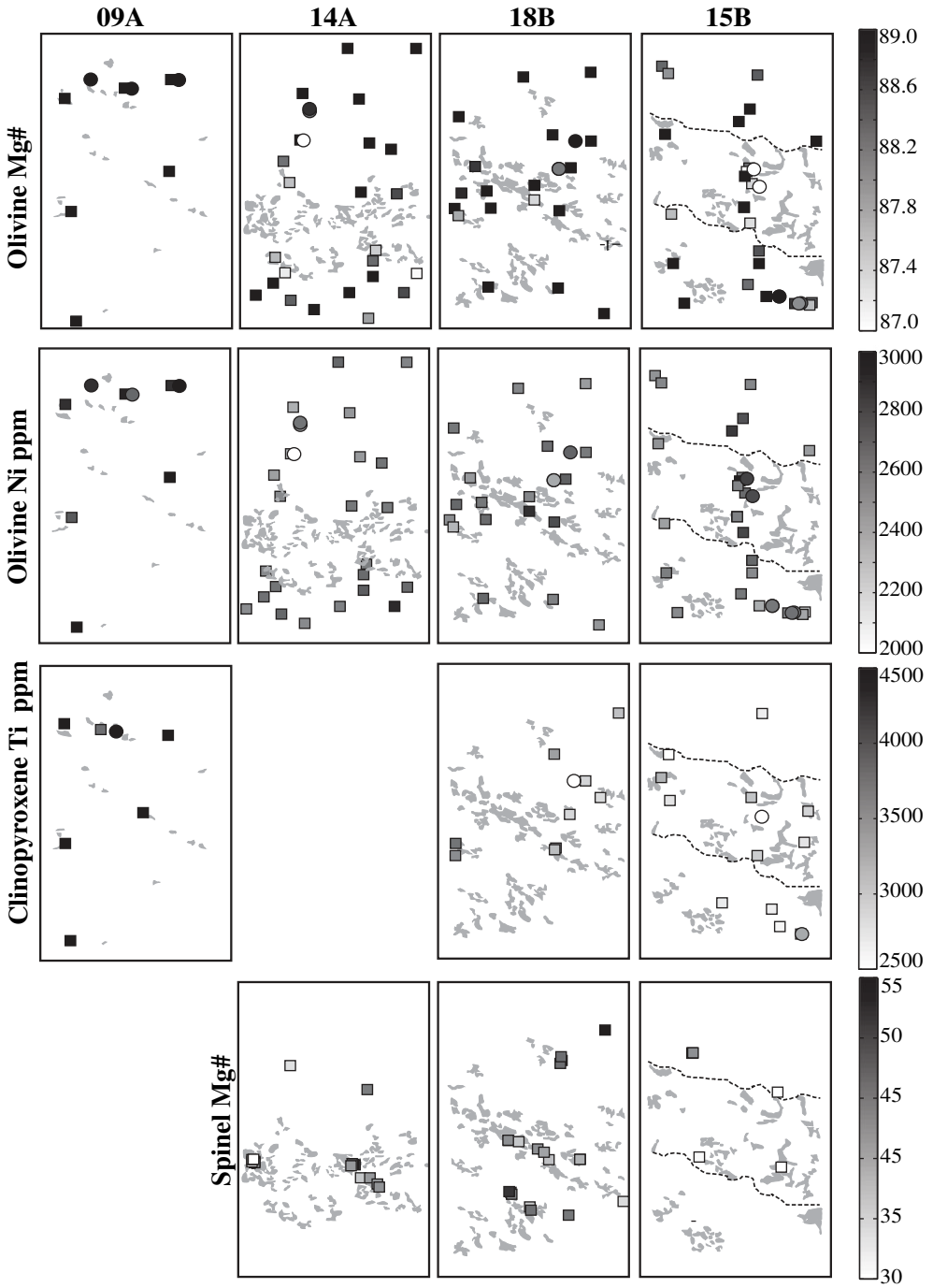

Fig. 10. Olivine Mg# and Ni content, clinopyroxene Ti content, and spinel Mg# plotted as a function of the analysis position in the sample to illustrate the relations between mineral compositions and local plagioclase content (indicated by the light grey patches). Squares represent data for mineral cores, circles for rims. No clinopyroxenes were analysed in sample 14 and no spinels in sample 9A.

5. Discussion

5.1. Synkinematic reactive melt percolation

Our observations corroborate previous studies in Central and South Lanzo (Bodinier et al., 1991; Kaczmarek and Muntener, 2008; Muntener and Piccardo, 2003; Piccardo et al., 2007), which interpreted the plagioclase layering as formed by reactive transport of melts at the base of a thinned mantle lithosphere. Microstructural evidence of melt–rock reaction, leading to crystallization of orthopyroxene, clinopyroxene, and plagioclase at the expense of olivine (refertilization), such as irregularly shaped orthopyroxenes enclosing olivine fragments with similar crystal orientations (Fig. 5c), is ubiquitous in the studied section. Refertilization reactions may also be inferred from the analysis of the modal compositions, which are enriched in clinopyroxene relative to partial melting trends (Fig. 3). The mineral chemistry, in particular the Fe-enrichment of olivine (Mg# < 88) and the high Cr# of spinel (>40) within or in the vicinity of the plagioclase-rich layers (Fig. 10), also supports that the compositional layering formed by reactive melt percolation. This interpretation is further corroborated by: (i) the absence of plagioclase enrichment in the pyroxenite bands relative to the surrounding peridotites and (ii) the interstitial to subhedral shapes of plagioclase crystals in the peridotites (Fig. 5b, f–h). Moreover, though some plagioclases display spinel cores (Fig. 5f), suggesting that they might have formed by solid-state reaction, most plagioclase in the peridotites is not associated with spinel (Fig. 5b, g).

Analysis of the relations between the layering, the deformation structures (SPO-defined foliation and lineation), and the CPO (Figs. 4 and 6) allows constraining the relative timing of deformation and melt percolation. The diffuse limits of the compositional layers (Fig. 2) preclude pre-kinematic reactive melt percolation, where the parallelism between the layering and the foliation would result from ductile transposition, as the latter process produces sharp limits between the layers. A diffuse compositional layering parallel to the foliation may, however, form synkinematically, if the melt distribution is controlled by the deformation, or post-kinematically, if the melt percolates preferentially along the pre-existing foliation planes (anisotropic percolation, cf. Le Roux et al., 2008; Tommasi et al., 2008; Waff and Faul, 1992).

The coexistence of microstructural evidence for reactive melt percolation, like the very irregular shapes and interpenetrating grain boundaries of both reactant and product phases, and of intracrystalline deformation features, such as the ubiquitous undulose extinction in all mineral phases, subgrains in olivine and kinks in orthopyroxene, and mechanical twins and crystal network bending in plagioclase (Fig. 5) clearly points, however, to synkinematic melt percolation, because if the two processes were not contemporaneous, the latter one would have erased the record of the other. Percolation of basaltic melts imply near solidus conditions and if it is post-kinematic, the association of high temperature and presence of interstitial melts results in fast annealing of the plastic deformation structures by restoration and static recrystallization processes. On the other hand, the interpenetrating grain boundaries produced by melt–rock reactions (e.g., the olivine–orthopyroxene grain boundaries in Fig. 5c–d) are not stable during plastic deformation, as the bulges tend to recrystallize into new grains at small strains.

Analysis of the CPO of the different mineral phases corroborates synkinematic refertilization reactions. Pyroxenes and plagioclase have CPOs that are consistent with the olivine CPO, but less concentrated (Figs. 6 and 8). The higher dispersion of the pyroxene CPO, in particular of clinopyroxene, and the obliquity of the plagioclase CPO relative to the olivine CPO and the layering suggest that these minerals accommodated lower finite strains by dislocation creep. These lower finite strains may be due to either a late-kinematic crystallization of some of the pyroxenes and plagioclase or to a higher contribution of diffusional processes to deformation in the partially molten peridotites.

5.2. Deformation processes in a partially molten mantle

The strong olivine and orthopyroxene CPO (Figs. 6 and 7), together with the ubiquitous undulose extinction in all mineral phases and the well-developed (100) subgrains in olivine and kinks in orthopyroxene (Fig. 5) are consistent with deformation by dominant dislocation creep. The coarse grain sizes, interpenetrating olivine–olivine grain boundaries (Fig. 5a), as well as the common 120° triple junctions (Fig. 5b,c) imply that dislocation creep was assisted by effective grain boundary migration, coherently with the inferred near-solidus deformation conditions. The presence of melt along grain boundaries may have favoured grain boundary migration, not only among single phase grain pairs, but also between different minerals, as interconnected melt may provide fast diffusion paths. However, the well-developed dislocation-related microstructures and the strong CPO of olivine indicate that melt fractions remained at all times below the solid matrix disruption threshold (20–40%; Rosenberg and Handy, 2005).

A characteristic feature of these plagioclase lherzolites is the predominance of olivine CPO with a strong axial-[010] tendency (BA index $\leq$ 0.35, Fig. 7a). Similar axial-[010] olivine CPO patterns were observed in the impregnated rocks from the Oman ophiolite crust–mantle transition zone (Fig. 7a; Higgie and Tommasi, 2012) and in refertilized peridotites from the Lherz and Ronda peridotite massifs (Le Roux et al., 2008; Soustelle et al., 2009). The observations in the Moho transition zone (MTZ) of the Oman ophiolite, in particular, clearly illustrate the relation between synkinematic melt fractions and olivine CPO, as the changes in olivine CPO symmetry occur at the mm-scale, as function of the modal composition of the layer (Fig. 7); dunitic layers have axial-[100] olivine CPO (BA > 0.65), whereas gabbroic layers have orthorhombic to [010]-axial patterns (BA < 0.65).

Axial-[010] olivine CPO patterns also developed in partially molten olivine aggregates deformed in simple shear when melt was homogeneously distributed as elongated pockets throughout the aggregate (Zimmerman et al., 1999). In contrast, in experiments where melt segregated, [010] concentrates normal to the shear plane, but [001] axes align in the shear direction (Holtzman et al., 2003b). The sum of observations on both natural and experimental systems points therefore to development of axial-[010] olivine CPO patterns favoured by deformation in the presence of melt.

In the present dataset, variations in the olivine CPO symmetry at the layer scale could not be clearly evidenced due to the diffuse character of the layering and the coarse grain sizes, which make the layers a few grains wide only, not allowing for a separated treatment of the olivine CPO data at the individual layer scale, and to the high degree of alteration of the plagioclase-rich bands, which hindered the measurement of the olivine CPO in these bands. However, olivine-rich layers from planar layering domains show systematically orthorhombic olivine CPO (Fig. 7a), whereas anastomosed layering domains show olivine CPO patterns ranging from strongly axial-[010] to orthorhombic (Fig. 7a).

Similar to the more common axial-[100] and orthorhombic olivine CPO, axial-[010] patterns may form in response to dominant activation of the [100](010) system, but the dispersion of both [100] and [001] axes in the foliation plane implies either additional activation of the [001](010) system (Tommasi et al., 2000) or 3D deformation, with stretching in multiple directions in the foliation plane (3D transpression; Tommasi et al., 1999). High pressure (Mainprice et al., 2005) or hydration (Jung and Karato, 2001; Mackwell et al., 1985) may favour the activation of [001](010). However, in the studied section, the crystallization of plagioclase implies low synkinematic pressures (<0.8 GPa, Borghini et al., 2010). In addition, in a partially molten system at low pressure, water would mainly partition into the melt (Hauri et al., 2006) and thus not strongly affect the deformation of olivine. Analysis of the orthopyroxene CPO indicates, nevertheless, that transpression may explain the axial-[010] olivine CPO patterns, since those samples showing the lowest BA-indexes, such as 21 and 12, have also orthopyroxene CPO characterized by dispersion of [001]

in the foliation plane (Fig. 6). Strain partitioning between melt-rich and melt-poor bands, with a component of layer normal shortening in addition to simple shear in the melt-rich bands, was already proposed to explain the changes in olivine CPO symmetry in the Oman MTZ, where this interpretation was supported by slight asymmetry relative to the layering displayed by the axial-[100] CPO, but not by the axial-[010] ones (Higgie and Tommasi, 2012).

In Lanzo, development of axial-[010] olivine CPO due to deformation in the presence of small melt fractions is also supported by the comparison between the olivine CPO measured in the study zone and those measured across the retrogressive shear zone that separates the Central and Northern bodies (Kaczmarek and Tommasi, 2011). Outside the shear zone, coarse-porphyroclastic plagioclase lherzolites from the Central body, which are very similar to those in the study area and display evidence for deformation under near-solidus conditions, have strong olivine CPO with an axial-[010] tendency, very similar to those in the present study area (BA indexes < 0.45, Fig. 7a). In contrast, fine-porphyroclastic and mylonitic peridotites from the shear zone, which deformed under sub-solidus, decreasing temperature conditions, show weaker olivine CPO with orthorhombic to axial-[100] patterns (BA indexes > 0.45 with a predominance of values > 0.6, Fig. 7a); the high dispersion of the olivine CPO in the mylonites (J-indexes < 4) is probably due to dynamic recrystallization. Finally, spinel peridotites from the Northern body, which is interpreted as an old lithospheric mantle fragment, less affected by melt percolation (Bodinier et al., 1991), show strong axial-[100] patterns (BA indexes > 0.65, J indexes > 6).

The pyroxene CPO is not changed by deformation in the presence of melt. The alignment of [001] in the layering plane, with a maximum subparallel to the olivine [100] maximum, and the concentration of [100] for orthopyroxene and of [010] for clinopyroxene normal to the layering (Fig. 6) is consistent with dislocation creep with dominant activation of the usual [001](100) and [001]{110} systems in enstatite and {110}[001] systems in clinopyroxene (Bascou et al., 2002; Frets et al., 2012; Green and Radcliffe, 1972). The slight obliquity (5–15°) of the pyroxenes CPO relative to the olivine CPO may result from lower shear strains accommodated by the pyroxenes due to their higher strength and/or from late-kinematic crystallization of a part of them. The latter process may also explain the dispersion of the clinopyroxene CPO. Late crystallization of at least a part of the pyroxenes is also suggested by their highly irregular shapes, characterized by grain boundaries with cusp shapes 'filling' triple junctions with olivine grains or even enclosing fragments of a previously unique olivine crystal (Fig. 5).

The plagioclase CPO is consistent with deformation by dislocation creep with dominant activation of the (010)[100] slip system (Fig. 8). However, plagioclase crystals show dominantly interstitial shapes and have low densities of intracrystalline deformation features (Fig. 5b,f–h), which are not consistent with high finite strains accommodated by solid-state deformation. An alternative explanation for the formation of this CPO, which was proposed by Higgie and Tommasi (2012) to explain the strong CPO of plagioclase and clinopyroxene with interstitial shapes in the gabbroic and intermediate composition layers in the Oman Ophiolite Moho transition zone (MTZ), is oriented crystallization in a deforming crystalline medium containing low melt fractions, where the alignment of the melt is controlled by the deformation.

5.3. Melt distribution controlled by deformation

Mineral compositions are more heterogeneous and more enriched in basaltic components in the plagioclase-rich domains (Fig. 9), suggesting interaction with variable melt volumes. The high Cr# of spinel in the plagioclase-rich layers probably records both near-solidus and sub-solidus re-equilibration with plagioclase and cannot be used to infer melt–rock interaction intensity. In contrast, as solid-state chemical re-equilibration results in homogenization of the Fe, Mg, and Ti contents, the strong heterogeneity in Mg# and in Ti content, which is preserved in the studied samples at the mm-scale, corroborates focusing of melt in the plagioclase-rich bands. In particular, the Fe-enrichment in olivine and spinel in the plagioclase-rich bands from the planar layering domains (Fig. 10) implies that these layers have interacted with larger melt volumes (e.g., Tommasi et al., 2004). The orthorhombic olivine CPO patterns in the planar layering domain (Fig. 7a) are also consistent with lower synkinematic melt fractions in the plagioclase-poor layers from this domain. Together, these data suggest that the planar layering domains record melt segregation in layers parallel to the shear plane.

Based on a similar association of microstructural and chemical data, we interpret the anastomosed layering, which is characterized by plagioclase-rich lenses or discontinuous layers a few grains wide aligned in the foliation, as recording melt distribution controlled by the deformation, but no melt segregation. The higher Ti contents in ortho- and clinopyroxenes from the anastomosed layering domains (Fig. 9b,c) may record local variations in the melt composition (local enrichment in Ti of the melt) due to the melt–rock reactions (e.g., Bodinier et al., 2008), suggesting less effective melt circulation, or trapped melt effects (e.g., Kaczmarek and Muntener, 2008). This interpretation is in agreement with the very high Ti contents in spinel (5000–8000 ppm, Fig. 9e) and low Mg# in pyroxenes from plagioclase-rich lenses in this domain. Variations in time and space in the melt content may also explain the strong variability of the olivine CPO symmetry within the diffuse anastomosed layering domain, the more axial-[010] patterns being associated with higher synkinematic melt fractions (integrated through time/strain).

Simple shear experiments in olivine aggregates containing low fractions of basaltic melts show either melt distributed in grain-scale pockets aligned at ~20° antithetically to the shear plane or segregated into melt-rich layers, which are several grains wide and form an interconnected anastomosed network with the main bands oriented at ~20° antithetically to the shear plane and the secondary bands subparallel to it (Holtzman and Kohlstedt, 2007; Holtzman et al., 2003a,b; King et al., 2010; Zimmerman et al., 1999). In these experiments, the transition between a homogeneous melt distribution to melt segregation is controlled by the compaction length of the system and by the finite strain; in experiments where the compaction length is significantly smaller than the sample size, segregation is observed at shear strains higher than one (King et al., 2010). An analysis of the mechanical behaviour in these experiments also shows a reduction in the shear viscosity, which may be accounted for by local reduction in strength and strain localization in the melt-rich bands (Holtzman et al., 2012).

Shear controlled melt organization, leading to melt segregation in layers subparallel to the shear plane has also been proposed to explain the centimetre to metre scale compositional layering and CPO of the main rock-forming minerals in the crust–mantle transition zone of the Oman ophiolite (Higgie and Tommasi, 2012; Jousselin et al., 2012) and the centimetre-scale pyroxenitic layering in the strongly deformed lherzolites far from the harzburgitic bodies in the Lherz massif (Le Roux et al., 2008). Both settings are characterized by high finite shear strains, recorded by the well-developed foliations and lineations and by the boudinage of the thicker pyroxenite layers in Lherz (Le Roux et al., 2008). In Lherz, lherzolites proximal to the harzburgites, which are less deformed, are not layered (Le Roux et al., 2008).

Together, observations in experimental and natural partially molten systems suggest that shear-induced melt segregation only occurs above a given finite strain. We may thus speculate that the predominance of a diffuse anastomosed layering implies low finite strains in most of the studied section, with the planar layering domains marking strain localization, may be associated with variations in the instantaneous melt fraction. However, there are no markers allowing the quantifying of variations in finite strain in the studied section. There is also no correlation between the layering morphology and the intensity of the olivine CPO. Similar olivine CPO intensities in spite of higher finite strains may, however, be accounted for if diffusion or grain boundary sliding accommodated part of the deformation in the melt-rich bands, as previously

proposed to explain the inconsistency between the macroscopic markers of strain and the CPO in the lherzolites of Lherz (Le Roux et al., 2008).

Finally, in the present study, as in the Oman MTZ or in the lherzolites from Lherz (Higgie and Tommasi, 2012; Le Roux et al., 2008), both plagioclase-rich lenses and layers are dominantly subparallel to the shear plane and not at ca. 20° to it as in the experiments (Holtzman et al., 2003a,b; King et al., 2010). As proposed by Higgie and Tommasi (2012), this difference may result from the much lower strain rates and stresses in nature relative to the experiments. An alternative explanation for this apparent discrepancy between experimental and natural observations was recently proposed by Soustelle et al. (2013) based on simple shear experiments on olivine + Si-rich melt assemblages. In these experiments, the orthopyroxenes produced by melt–rock reaction are oriented parallel to the shear plane, but the residual melt pockets are oriented at ~20° from it, leading Soustelle et al. (2013) to propose that melts initially concentrate along the crystal interfaces in extension, but stress concentration and preferential recrystallization resulted in higher reaction rates along the compressional interfaces, with post-crystallization shearing producing the final alignment of the reaction products with the shear plane. However, melt segregation was not observed in these experiments.

5.4. Consequences to the mantle seismic and mechanical properties

Development of a preferred orientation of melt-rich lenses forming an anastomosed network or layers subparallel to the shear plane will result in a strong anisotropy of the upper mantle physical properties. The seismic anisotropy of a partially molten peridotite may be estimated by a method that associates the Gassman poro-elastic approach at low frequencies with a differential effective medium approach at high frequencies (Mainprice, 1997). Even at melt fractions as low as 2%, the presence of melt pockets flattened in the foliation plane with aspect ratios of 5:5:1, which are consistent with the shapes of the plagioclase-rich lenses in the anastomosed layering domain (Fig. 4), results in an almost transverse isotropic pattern with a slow symmetry axis (Tommasi et al., 2006; Vauchez et al., 2000). This results in low P- and S-wave velocities and weak S-wave birrefringence for waves propagating normal to the foliation and in a high birefringence for S-waves propagating parallel to it. The intensity of the seismic anisotropy and its transverse isotropy symmetry are strongly enhanced for increasing aspect ratios of the melt pockets and melt fractions (Tommasi et al., 2006; Vauchez et al., 2000).

Development of a network of melt-rich layers parallel to the shear plane will thus induce an impedance contrast for waves propagating at high angles to the melt layering that may account for the strong receiver function signal observed at depths corresponding to the lithosphere–asthenosphere boundary in many locations worldwide (e.g., Kawakatsu et al., 2009; Rychert and Shearer, 2009). It may also produce the strong SKS splitting observed in the East African rift, if the melt pockets or lenses are oriented vertically (Kendall et al., 2005).

This process may also produce strong anisotropy in: (i) permeability, with an enhanced permeability along the shear plane (Rosenberg and Handy, 2000; Takei and Holtzman, 2009), and (ii) viscosity, with a significant reduction of the resistance to layer-parallel shearing (Holtzman et al., 2012). It could therefore provide a mechanism whereby melt lubrication would localize deformation at plate boundaries (Holtzman and Kendall, 2010).

The seismic signature of deformation in the presence of melt may be preserved even after the total crystallization of the system, as it changes the olivine CPO patterns. Axial-[010] olivine CPO results in low S-wave birrefringence (apparent isotropy) normal to the flow plane (Bascou et al., 2008; Tommasi et al., 2008). This contrasts with the upper mantle seismic anisotropy associated with orthorhombic or axial-[100] olivine CPO, which are the typical olivine CPO developed by deformation by dislocation creep under dry conditions in the upper 200 km of the mantle (<200–250 km depth), where the apparent isotropy direction is subparallel to the flow direction (Mainprice et al., 2005; Tommasi et al., 2000).

6. Conclusions

Petrostructural analysis of the plagioclase lherzolites from the northwestern part of the Central Lanzo peridotite body shows that the compositional layering results from synkinematic reactive melt percolation, during which the melt distribution is controlled by the deformation. Evidence for coeval deformation and melt percolation comprises: (i) the parallelism between the layering, the foliation and lineation marked by the olivine SPO, and the CPOs of all rock-forming minerals, (ii) the diffuse limits of the layers, and (iii) the coexistence of microstructural evidence for melt–rock reactions (interpenetrating phase boundaries) and for deformation by dislocation creep (undulose extinction, subgrains in olivine, kinks in orthopyroxene). Deformation in the presence of melt is also suggested by the coarse grain sizes, the microstructural evidence for effective grain boundary migration (sinuous or polygonal olivine grain boundaries), and the predominance of axial-[010] olivine CPO, which has been systematically observed both in experiments and in other peridotites deformed in the presence of melt. However, the strong CPO and microstructural evidence for dislocation creep in olivine and pyroxenes implies that instantaneous melt fractions remained low ($\ll$20–30%).

The most characteristic feature of the studied section is the variation in morphology of the layering. The dominant pervasive anastomosed network of plagioclase-rich bands with diffuse limits, a few millimetres to centimetres wide, enclosing plagioclase-poor lenses, grades locally into a planar layering formed by the alternation of plagioclase-rich or poor bands a few centimetres to tens of centimetres wide. The heterogeneity of mineral compositions in the planar layering domains, in particular the Fe-enrichment in olivine and spinel and the Ti content in spinel in the plagioclase-rich bands, implies that these layers have interacted with larger melt volumes than the olivine-rich ones. This suggests melt focusing in these layers. On the other hand, the marked enrichment in Ti in pyroxenes and spinel and the low Mg# in pyroxenes in the plagioclase-rich lenses of the anastomosed layering domain implies local variations in the melt composition, suggesting a less effective circulation, or trapped-melt effects. We conclude therefore that the planar layering records melt segregation in layers parallel to the shear plane, whereas the anastomosed layering results from a more homogeneous melt distribution, in which melt aligns preferentially along grain boundaries subparallel to the shear plane. Although finite strain variations between layers cannot be quantified, we speculate, based on comparison with data from experiments, which show both melt segregation as a function of finite strain and reduction in shear viscosity due to the segregation, and from other mantle outcrops displaying shear-controlled melt organization, that the transition from the anastomosed to the planar layering records an increase in finite strain, that is, strain localization associated with variations in the instantaneous melt fraction.

This study corroborates that in a deforming mantle, the melt distribution is controlled by the deformation and that this process does not require high melt fractions. The alignment of melt pockets or, at high strains, melt segregation in the shear plane will produce a marked anisotropy in the mantle physical properties, notably a reduction of the shear viscosity parallel to the layering and a seismic anisotropy characterized by a transverse isotropy with a slow symmetry axis.

Supplementary data to this article can be found online at http://dx.doi.org/10.1016/j.tecto.2014.01.007.

Acknowledgements

This work significantly benefited from frequent discussions with A. Vauchez, F. Boudier, and J.L. Bodinier and from constructive reviews by O. Muntener and an anonymous reviewer. We thank A. Vauchez, C. Cavalcante and L.G. Viegas for help in the field. D. Mainprice provided

softwares and advice for analysing/plotting CPO data. C. Nevado and D. Delmas supplied high quality polished thin sections for EBSD measurements. F. Barou helped with EBSD data acquisition. Electron microprobe analyses were carried out with the help of C. Merlet at the Service Microsonde Sud, Université Montpellier 2. The research leading to these results has been funded by the Initial Training Network (ITN) Crystal2Plate, an FP7-funded Marie Curie Action under grant agreement number PITN-GA-2008-215353. The EBSD-SEM national facility in Montpellier is supported by the Institut National de Sciences de l'Univers (INSU) du Centre National de la Recherche Scientifique (CNRS), France and by the Conseil Régional Languedoc-Roussillon, France.

References

Bachmann, F., Hielscher, R., Jupp, P.E., Pantleon, W., Schaeben, H., Wegert, E., 2010. Inferential statistics of electron backscatter diffraction data from within individual crystalline grains. J. Appl. Crystallogr. 43, 1338–1355.

Bascou, J., Tommasi, A., Mainprice, D., 2002. Plastic deformation and development of clinopyroxene lattice preferred orientations in eclogites. J. Struct. Geol. 24, 1357–1368.

Bascou, J., Delpech, G., Vauchez, A., Moine, B.N., Cottin, J.Y., Barruol, G., 2008. An integrated study of microstructural, geochemical, and seismic properties of the lithospheric mantle above the Kerguelen plume (Indian Ocean). Geochem. Geophys. Geosyst. 9 Q04036.

Ben Ismail, W., Mainprice, D., 1998. An olivine fabric database: an overview of upper mantle fabrics and seismic anisotropy. Tectonophysics 296, 145–157.

Bodinier, J.L., 1988. Geochemistry and petrogenesis of the Lanzo peridotite body, western Alps. Tectonophysics 149, 67–88.

Bodinier, J.-L., Menzies, M.A., Thirlwall, M.F., 1991. Continental to oceanic mantle transition — REE and Sr–Nd isotopic geochemistry of the Lanzo lherzolite massif. J. Petrol. 191–210 (Special Lherzolite Issue).

Bodinier, J.L., Garrido, C.J., Chanefo, I., Bruguier, O., Gervilla, F., 2008. Origin of pyroxenite–peridotite veined mantle by refertilization reactions: evidence from the Ronda peridotite (southern Spain). J. Petrol. 49, 999–1025.

Borghini, G., Fumagalli, P., Rampone, E., 2010. The stability of plagioclase in the upper mantle: subsolidus experiments on fertile and depleted lherzolite. J. Petrol. 51, 229–254.

Boudier, F., 1978. Structure and petrology of the Lanzo peridotite massif (Piedmont Alps). Geol. Soc. Am. Bull. 89, 1574–1591.

Brown, M., Solar, G.S., 1998. Shear-zone systems and melts: feedback relations and self-organization in orogenic belts. J. Struct. Geol. 24 (20), 211–227.

Bunge, H.J., 1982. Texture Analysis in Materials Science. Buttleworth, London.

Caricchi, L., Gaillard, F., Mecklenburgh, J., Le Trong, E., 2011. Experimental determination of electrical conductivity during deformation of melt-bearing olivine aggregates: implications for electrical anisotropy in the oceanic low velocity zone. Earth Planet. Sci. Lett. 302, 81–94.

Compagnoni, R., Sandrone, R., 1979. Il massicio di Lanzo nel quadro del metamorphismo alpino. Soc. Ital. Mineral. Petrol. 35.

Dijkstra, A.H., Drury, M.R., Vissers, R.L.M., Newman, J., 2002. On the role of melt–rock reaction in mantle shear zone formation in the Othris peridotite massif (Greece). J. Struct. Geol. 24, 1431–1450.

Frets, E., Tommasi, A., Garrido, C.J., Padrón-Navarta, J.A., Amri, I., Targuisti, K., 2012. Deformation processes and rheology of pyroxenites under lithospheric mantle conditions. J. Struct. Geol. 39, 138–157.

Green, H., Radcliffe, S., 1972. Deformation processes in the upper mantle. Geoph. Mono Series 16, 139–156.

Hauri, E.H., Gaetani, G.A., Green, T.H., 2006. Partitioning of water during melting of the Earth's upper mantle at H_2O-undersaturated conditions. Earth Planet. Sci. Lett. 248, 715–734.

Hielscher, R., Schaeben, H., 2008. A novel pole figure inversion method: specification of the MTEX algorithm. J. Appl. Crystallogr. 41, 1024–1037.

Higgie, K., Tommasi, A., 2012. Feedbacks between deformation and melt distribution in the crust–mantle transition zone of the Oman ophiolite. Earth Planet. Sci. Lett. 359–360, 61–72.

Hollister, L.S., Crawford, M.L., 1986. Melt-enhanced deformation: a major tectonic process. Geology 14, 558–561.

Holtzman, B.K., Kendall, J.M., 2010. Organized melt, seismic anisotropy, and plate boundary lubrication. Geochem. Geophys. Geosyst. 11, Q0AB06.

Holtzman, B.K., Kohlstedt, D.L., 2007. Stress-driven melt segregation and strain partitioning in partially molten rocks: effects of stress and strain. J. Petrol. 48, 2379–2406.

Holtzman, B.K., Groebner, N.J., Zimmerman, M.E., Ginsberg, S.B., Kohlstedt, D.L., 2003a. Stress-driven melt segregation in partially molten rocks. Geochem. Geophys. Geosyst. 4, 8607.

Holtzman, B.K., Kohlstedt, D.L., Zimmerman, M.E., Heidelbach, F., Hiraga, T., Hustoft, J., 2003b. Melt segregation and strain partitioning: implications for seismic anisotropy and mantle flow. Science 301, 1227–1230.

Holtzman, B.K., Kohlstedt, D.L., Morgan, J.P., 2005. Viscous energy dissipation and strain partitioning in partially molten rocks. J. Petrol. 46, 2569–2592.

Holtzman, B.K., King, D.S., Kohlstedt, D.L., 2012. Effects of stress-driven melt segregation on the viscosity of rocks. Earth Planet. Sci. Lett. 359, 184–193.

Jousselin, D., Morales, L.F.G., Nicolle, M., Stephant, A., 2012. Gabbro layering induced by simple shear in the Oman ophiolite Moho transition zone. Earth Planet. Sci. Lett. 331–332, 55–66.

Jung, H., Karato, S.-I., 2001. Water-induced fabric transitions in olivine. Science 293, 1460–1463.

Kaczmarek, M.-A., Muntener, O., 2008. Juxtaposition of melt impregnation and high-temperature shear zones in the upper mantle: field and petrological constraints from the Lanzo peridotite (northern Italy). J. Petrol. 49, 2187–2220.

Kaczmarek, M.-A., Tommasi, A., 2011. Anatomy of an extensional shear zone in the mantle, Lanzo massif, Italy. Geochem. Geophys. Geosyst. 12, Q0AG06.

Kaczmarek, M.A., Müntener, O., Rubatto, D., 2008. Trace element chemistry and U–Pb dating of zircons from oceanic gabbros and their relationship with whole rock composition (Lanzo, Italian Alps). 295–312.

Katz, R.F., Spiegelman, M., Holtzman, B., 2006. The dynamics of melt and shear localization in partially molten aggregates. Nature 442, 676–679.

Kawakatsu, H., Kumar, P., Takei, Y., Shinohara, M., Kanazawa, T., Araki, E., Suyehiro, K., 2009. Seismic evidence for sharp lithosphere–asthenosphere boundaries of oceanic plates. Science 324, 499–502.

Kelemen, P.B., Dick, H.J.B., 1995. Focused melt flow and localized deformation in the upper mantle: juxtaposition of replacive dunite and ductile shear zones in the Josephine peridotite, SW Oregon. J. Geophys. Res. 100, 423–438.

Kendall, J.M., Stuart, G.W., Ebinger, C.J., Bastow, I.D., Keir, D., 2005. Magma-assisted rifting in Ethiopia. Nature 433, 146–148.

Kienast, J.R., Pognante, U., 1988. Chloritoid-bearing assemblages in eclogitised metagabbros of the Lanzo peridotite body (western Italian Alps). Lithos 21, 1–11.

King, D.S.H., Zimmerman, M.E., Kohlstedt, D.L., 2010. Stress-driven melt segregation in partially molten olivine-rich rocks deformed in torsion. J. Petrol. 51, 21–42.

Lagabrielle, Y., Fudral, S., Kienast, J.-R., 1989. La couverture océanique des ultrabasites de Lanzo (Alpes occidentales): arguments lithostratigraphiques et pétrologiques (The oceanic cover of the Lanzo peridotite body (western Italian Alps): lithostratigraphic and petrological evidences). Geodin. Acta 3, 43–55.

Le Roux, V., Tommasi, A., Vauchez, A., 2008. Feedback between melt percolation and deformation in an exhumed lithosphere–asthenosphere boundary. Earth Planet. Sci. Lett. 274, 401–413.

Mackwell, S.J., Kohlstedt, D.L., Paterson, M.S., 1985. The role of water in the deformation of olivine single crystals. J. Geophys. Res. 90, 11319–11333.

Mainprice, D., 1997. Modelling anisotropic seismic properties of partially molten rocks found at mid-ocean ridges. Tectonophysics 279, 161–179.

Mainprice, D., Tommasi, A., Couvy, H., Cordier, P., Frost, D.J., 2005. Pressure sensitivity of olivine slip systems and seismic anisotropy of Earth's upper mantle. Nature 433, 731–733.

Mainprice, D., Hielscher, R., Schaeben, H., 2011. Calculating anisotropic physical properties from texture data using the MTEX open-source package. Geol. Soc. Lond. Spec. Publ. 360, 175–192.

Muntener, O., Piccardo, G.B., 2003. Melt migration in ophiolitic peridotites: the message from Alpine–Apennine peridotites and implications for embryonic ocean basins. Geol. Soc. Lond. Spec. Publ. 218, 69–90.

Niu, Y., Langmuir, C.H., Kinzler, R.J., 1997. The origin of abyssal peridotites: a new perspective. Earth Planet. Sci. Lett. 152, 251–265.

Pelletier, L., Müntener, O., 2006. High-pressure metamorphism of the Lanzo peridotite and its oceanic cover, and some consequences for the Sesia–Lanzo zone (northwestern Italian Alps). Lithos 90, 111–130.

Piccardo, G.B., Zanetti, A., Muntener, O., 2007. Melt/peridotite interaction in the Southern Lanzo peridotite: field, textural and geochemical evidence. Lithos 94, 181–209.

Rosenberg, C.L., Handy, M.R., 2000. Syntectonic melt pathways during simple shearing of a partially molten rock analogue (norcamphor–benzamide). J. Geophys. Res. 105, 3135–3149.

Rosenberg, C.L., Handy, M.R., 2005. Experimental deformation of partially melted granite revisited: implications for the continental crust. J. Metamorph. Geol. 23, 19–28.

Rubatto, D., Müntener, O., Barnhoorn, A., Gregory, C., 2008. Dissolution–reprecipitation of zircon at low-temperature, high-pressure conditions (Lanzo massif, Italy). Am. Mineral. 93, 1519–1529.

Rychert, C.A., Shearer, P.M., 2009. A global view of the lithosphere–asthenosphere boundary. Science 324, 495–498.

Soustelle, V., Tommasi, A., Bodinier, J.L., Vauchez, A., Garrido, C.J.M., 2009. Deformation and reactive melt transport in the mantle lithosphere above a partial melting domain (Ronda peridotite massif, Spain). J. Petrol. 50, 1235–1266.

Soustelle, V., Walte, N.P., Manthilake, M.G.M., Frost, D.J., 2013. Melt migration and melt–rock reactions in the deforming Earth's upper mantle: experiments at high pressure and temperature. Geology G34889-1. http://dx.doi.org/10.1130/G34889.1.

Takei, Y., 2005. Deformation-induced grain boundary wetting and its effects on the acoustic and rheological properties of partially molten rock analogue. J. Geophys. Res. 110, B12203.

Takei, Y., Holtzman, B.K., 2009. Viscous constitutive relations of solid–liquid composites in terms of grain boundary contiguity: 3. Causes and consequences of viscous anisotropy. J. Geophys. Res. 114, B06207.

Tommasi, A., Vauchez, A., Femandes, L.A.D., Porcher, C.C., 1994. Magma-assisted strain localization in an orogen-parallel transcurrent shear zone of southern Brazil. Tectonics 13, 421–437.

Tommasi, A., Tikoff, B., Vauchez, A., 1999. Upper mantle tectonics: three-dimensional deformation, olivine crystallographic fabrics and seismic properties. Earth Planet. Sci. Lett. 168, 173–186.

Tommasi, A., Mainprice, D., Canova, G., Chastel, Y., 2000. Viscoplastic self-consistent and equilibrium-based modeling of olivine lattice preferred orientations: implications for the upper mantle seismic anisotropy. J. Geophys. Res. 105, 7893–7908.

Tommasi, A., Godard, M., Coromina, G., Dautria, J.-M., Barsczus, H., 2004. Seismic anisotropy and compositionally induced velocity anomalies in the lithosphere above mantle plumes: a petrological and microstructural study of mantle xenoliths from French Polynesia. Earth Planet. Sci. Lett. 227, 539–556.

Tommasi, A., Vauchez, A., Godard, M., Belley, F., 2006. Deformation and melt transport in a highly depleted peridotite massif from the Canadian Cordillera: implications to seismic anisotropy above subduction zones. Earth Planet. Sci. Lett. 252, 245–259.

Tommasi, A., Vauchez, A., Ionov, D.A., 2008. Deformation, static recrystallization, and reactive melt transport in shallow subcontinental mantle xenoliths (Tok Cenozoic volcanic field, SE Siberia). Earth Planet. Sci. Lett. 272, 65–77.

Ulrich, S., Mainprice, D., 2005. Does cation ordering in omphacite influence development of lattice-preferred orientation? J. Struct. Geol. 27, 419–431.

Vauchez, A., Tommasi, A., Barruol, G., Maumus, J., 2000. Upper mantle deformation and seismic anisotropy in continental rifts. Phys. Chem. Earth Solid Earth Geod. 25, 111–117.

Vollmer, F.W., 1990. An application of eigenvalue methods to structural domain analysis. Geol. Soc. Am. Bull. 102, 786–791.

Waff, H.S., Faul, U.H., 1992. Effects of crystalline anisotropy on fluid distribution in ultramafic partial melts. J. Geophys. Res. 97, 9003–9014.

Walter, M.J., Sisson, T.W., Presnall, D.C., 1995. A mass proportion method for calculating melting reactions and application to melting of model upper mantle lherzolite. Earth Planet. Sci. Lett. 135, 77–90.

Zimmerman, M.E., Zhang, S., Kohlstedt, D.L., Karato, S., 1999. Melt distribution in mantle rocks deformed in shear. Geophys. Res. Lett. 26, 1505–1508.